Applied Catalysis B: Environmental 310 (2022) 121063

Contents lists available at ScienceDirect

Applied Catalysis B: Environmental

journal homepage: www.elsevier.com/locate/apcatb

Solar light-induced injection of hot electrons and photocarriers for synergistically enhanced photothermocatalysis over Cu-Co/$SrTiO_3$ catalyst towards boosting CO hydrogenation into C2–C4 hydrocarbons

Shangbo Ning [a], Yanhui Sun [a], Shuxin Ouyang [b,*], Yuhang Qi [a], Jinhua Ye [a,c,**]

[a] TJU-NIMS International Collaboration Laboratory, School of Materials Science and Engineering, Tianjin University, No. 92 Weijin Road, Nankai District, Tianjin 300072, China
[b] College of Chemistry, Central China Normal University, No. 152, Luoyu Road, Wuhan 430079, China
[c] International Center for Materials Nanoarchitectonics (WPI-MANA), National Institute for Materials Science (NIMS), 1-1 Namiki, Tsukuba 305-0047, Japan

ARTICLE INFO

Keywords:
Solar light
Photocatalysis
Photothermocatalysis
Synergistically enhanced effect
Cu, Co co-loaded $SrTiO_3$

ABSTRACT

Solar light-driven catalysis provides a viable approach for solar-to-chemical energy conversion, but it is difficult to maximize the conversion efficiency of solar energy through individual photocatalysis or photothermocatalysis. Herein, we construct a light-induced photo- and thermal-synergistic catalysis based on an adjacent Co and Cu nanoparticles co-loading on $SrTiO_3$ nanoparticles. Under the irradiation of concentrated solar light, the $SrTiO_3$ support is excited by ultraviolet light to induce photocatalytic effect to generate photocarriers; meanwhile, the localized surface plasma resonance-active Cu nanoparticles mainly absorb the visible-infrared light to produce hot electrons which are either quenched to generate heat or transported to active sites; finally, the active-phase Co nanoparticles converge the electrons and heat to drive CO hydrogenation into C2–C4 hydrocarbons. This study demonstrates that a rationally-designed catalyst can effectively convert solar energy to photocarriers/hot electrons and heat, and importantly, can couple them to regulate reaction pathways towards the production of value-added chemicals.

1. Introduction

Efficient utilization and conversion of solar energy is regarded as one of the most promising approaches to address the ever-growing energy challenge [1–4]. Except for applying photoelectric conversion via solar cell [4,5], photocatalysis and photothermocatalysis provide a way to directly convert solar energy into chemical energy which is suitable for storage, transport and utilization [2,6,7]. In general, photocatalysis takes advantage of the efficient utilization of ultraviolet (UV) and visible light [8–10]; to extend solar spectral utilization, a few photocatalysts were developed to respond to near-infrared (NIR) light [11,12]. Compared with photocatalysis with the absorption limitation of sunlight spectrum, photothermocatalysis can achieve near full spectral absorption and therefore has more potential to deliver more efficient solar conversion, which has recently drawn great research interests [13–15].

Among the NIR light-responsive photocatalysts currently being investigated, both the intrinsic absorption of the catalyst and the localized surface plasma resonance (LSPR) effect of nano-metal nanoparticles generate the low-energy carriers but exhibit the strong thermal effect (which is caused by carrier quenching) [16], thus resulting in relatively low photocatalytic activity [17]. Interestingly, photothermal catalysts with full solar spectral absorption can effectively convert light to thermal energy to drive thermocatalysis reaction. In recent years, the study demonstrated that the surface temperature of the group VIII metal nanoparticles increased above 300 °C within a few minutes under concentrated solar-light irradiation (simulated by Xe lamp), which achieved excellent photothermocatalytic performance [18,19]. However, with the in-depth study of photothermocatalysis, in addition to light-to-thermal conversion emphatically proceeds, the influence of manipulating electron transfer effect on the reactivity and selectivity in photothermocatalysis has been revealed. Zhang and colleagues pioneeringly reported that electrons transfer from MnO oxide to the Ni^0 is

* Corresponding author at: College of Chemistry, Central China Normal University, No. 152, Luoyu Road, Wuhan 430079, China.
** Corresponding author at: TJU-NIMS International Collaboration Laboratory, School of Materials Science and Engineering, Tianjin University, No. 92 Weijin Road, Nankai District, Tianjin 300072, China.
E-mail addresses: oyxs@mail.ccnu.edu.cn (S. Ouyang), jinhua.ye@nims.go.jp (J. Ye).

https://doi.org/10.1016/j.apcatb.2022.121063
Received 21 October 2021; Received in revised form 15 December 2021; Accepted 2 January 2022
Available online 7 January 2022

responsible for modifying the electronic structure of nickel [20], thereby improving the CO hydrogenation selectivity toward light olefins. Recently, we found that the high energy photoholes from $SrTiO_3$ can improve the CO hydrogenation capacity, and photoelectrons can be beneficial to C-C coupling on Co nanoparticles [21]. These concepts of photothermal catalyst design inspire us to optimally utilize solar energy uniquely as the energy input to achieve light-induced injection of hot electrons and photocarriers for synergistically enhanced photothermocatalysis.

To construct such a catalyst, a simple microstructural configuration of adjacent nano-metals loaded semiconductor catalyst is proposed as follows: the semiconductor support can act as a donor of photogenerated carriers through the effect of photocatalysis [22]; the LSPR-active metal nanoparticles can bifunctionally work for light-to-thermal conversion and serve as a hot-electron donor; the active-phase metal nanoparticles can be coupling to the LSPR-active metal nanoparticle towards accumulate light-induced electrons and heat to drive superior catalysis. The UV–visible-infrared (UV–visible-IR) light can be harvested by this catalyst to carry out a photo- and thermal-synergistic catalysis through a different mechanism (Scheme 1a). Taking solar-driven CO hydrogenation as an example, the reduction process is expected to be promoted (Scheme 1b). Among many wide-band-gap semiconductor photocatalysts, $SrTiO_3$ is chosen as the support, because of its suitable valence band and conduction band position, it is widely regarded as the photogenerated carriers donor that drive the redox of H_2O [9,23]. As for the LSPR-active nano-metal, the earth-abundant and low-cost Cu is selected, because Cu nanoparticles can achieve prominent light-to-thermal effect [24] and hot-electrons export induced by visible-IR light [25]. In general, Co-based catalysts have the ability to drive CO low-temperature hydrogenation. Metallic Co as the active sites of Fischer-Tropsch synthesis (FTS) is a feasible strategy [26]. The well-constructed interface among Cu, Co, and $SrTiO_3$ is essential for the fluent transfer of electrons and heat, which facilitates the light-induced enhanced photo- and thermal-synergistic catalysis.

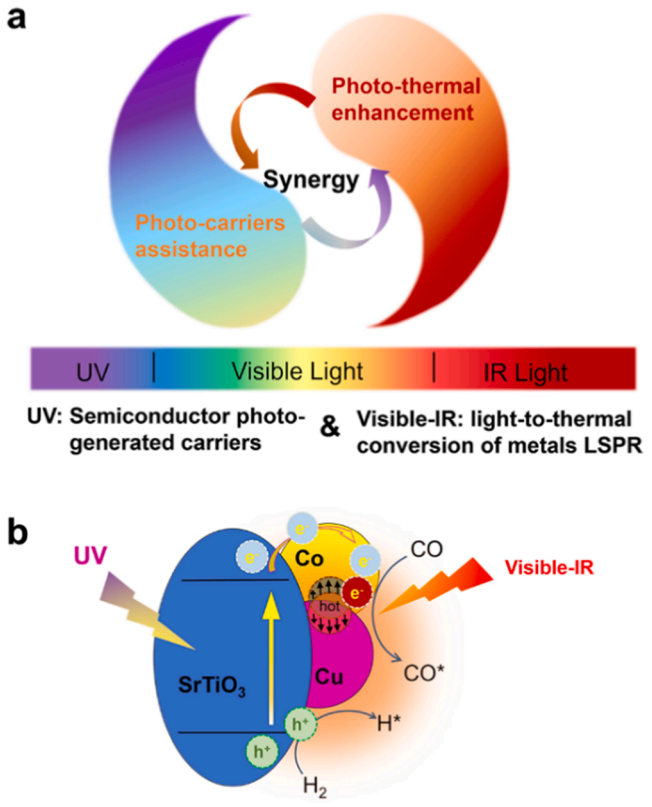

Scheme 1. Schematic illustration of the designed light-induced enhanced photo- and thermal-synergistic catalysis for CO hydrogenation.

In this work, by regulating Cu and Co nanoparticles on the $SrTiO_3$ nanoparticles, the solar light-induced enhanced photo- and thermal-synergistic catalysis can be achieved. When the individual thermocatalysis and photocatalysis occurred over the Cu-Co/STO catalyst, the CO conversion mainly underwent the water-gas shift (WGS) reaction and CO methanation, respectively. However, under full-spectrum irradiation from concentrated solar light, the CO reduction over the Cu-Co/STO catalyst shifted to FTS to produce C2–C4 hydrocarbons. The optimized photothermal catalyst of 1.5Cu-2Co/STO delivered an efficient yield of C2–C4 hydrocarbons with a total organic carbon (TOC) rate of 1.36 mmol g^{-1} h^{-1}, and the selectivity of C2–C4 reached 53.4% which was nearly 1.5- and 17.2-fold enhancement compared with 2Co/STO and 1.5Cu/STO, respectively, which clearly indicates the synergistic effect among Co, Cu, and $SrTiO_3$. Apparently, the rational design of photocatalyst to achieve light-induced enhanced photo- and thermal-synergistic catalysis can govern the reaction pathway to convert solar energy towards value-added chemicals.

2. Experimental section

The details on chemicals and materials, and characterization of catalysts are described in the Supporting information.

2.1. Synthesis of catalysts

The 2Co/STO was prepared according to a previous report [21]. Three-component Cu-Co/STO nanoparticles were synthesized based on an as-prepared 2Co/STO sample. First, the 2Co/STO nanoparticles were impregnated with an aqueous solution of $Cu(NO_3)_2$. Afterwards, the precursor solution was stirred at 120 °C, heated at reflux for 2 h, and then dried at 80 °C overnight. Finally, the powder was calcined at 300 °C for 2 h in an atmosphere of mixed gases Ar and H_2 (9: 1; v/v) to obtain yCu-2Co/STO product (the y% signifies the weight ratio of Cu^{2+} to Co/STO, y% = 0.3%, 0.7%, 1.1%, 1.3%, 1.5%, 1.7%, 2%, 3% and 5%). As reference sample, 1.5Cu/STO was prepared by the same method. In addition, the Co/STO sample was impregnated in Cu^{2+} of 1.5% solution, and the 1.5Cu-2Co/STO-PD was finally obtained by Xe lamp light-deposition. The 1.5Cu-2Co/STO-300D and 1.5Cu-2Co/STO-700D catalysts were obtained by one-step calcination and reduction of Cu^{2+}, Co^{2+} and STO mixture precursors at 300 °C and 700 °C, respectively.

2.2. Catalytic activity

The photo-driven catalytic evaluation of the catalyst was carried out in a closed, circulating glass reactor. The lamp irradiation (light intensity, 1.2 W cm^{-2}) of a 300 W Xe lamp was used as the energy to drive the reaction. 100 mg of the as-prepared catalysts was evenly spread on the quartz filter plate of the reactor with an area of ~ 7.0 cm^{-2}. After evacuating the reaction system, a certain amount of mixed gas of H_2 and CO was sequentially injected into the system (H_2: CO = 2: 1; v/v, P_{total} = 65 kPa). The contrast experiments of light-driven catalytic performance over the Cu-Co/STO were obtained (visible-IR light: ≥ 400 nm (UV-cutoff filter); UV light: ≤ 400 nm (visible-IR-cutoff filter)). Gas chromatograph (GC-2014 C, Shimadzu Co, Japan) and two gas analysis channels were used to detect reaction products and CO reactants. One of the channels was connected to the methanizer by flame ionization detector (FID), and analyzed CO and CO_2 in N_2 carrier gas. The other channel used FID in N_2 carrier gas for the determination of organic-carbon products.

2.3. Light-to-thermal conversion study

The thermocouple and infrared thermal imaging were used to test the temperature of catalytic materials surface under light irradiation in

the reaction atmosphere (H_2: CO = 2: 1) to study the photothermal conversion efficiency. The prepared catalysts were uniformly dispersed on the quartz filter plate with an area of ~ 7.0 cm^{-2}. At the light irradiation distance of about 10 cm, the infrared temperature probe or thermocouple detected the temperature during the reaction process. In addition, the surface temperature of the catalysts was regularly recorded.

2.4. *In situ light/thermal-chemical DRIFTS study*

In-situ diffuse reflectance infrared Fourier transform spectroscopy (DRIFTS) was measured by the Nicolet 6700 instrument, using an infrared cell unit connected to the ventilation device. In a mixed atmosphere (H_2: CO = 2: 1, flow rate 20 mL min^{-1}), the evolution process of active species on the catalyst surface under light irradiation and thermocouple heating was studied. The temperature reached 290 °C under the coordinated effect of light and heat to detect the adsorbed surface species, and compare it with a thermal driven reaction at 290 °C. For the collaborative photothermal effect, the temperature of driving reaction cannot be reached under the irradiation of a sole Xe lamp because the sample platform of the detection cell was far from the light irradiation window. To ensure that the temperature of sample reached 290 °C, it was necessary to conduct light irradiation and thermocouple assisted heating on the sample platform.

3. Results and discussion

3.1. *Formation and characterization of Cu and Co co-loaded $SrTiO_3$*

The Cu-Co/STO catalysts were obtained by a two-step reduction of Co^{2+} and Cu^{2+} impregnated STO with a simple thermal treatment technique (Fig. 1a). The first step thermal reduction is to load the Co nanoparticles on the STO surface. The 2Co/STO catalyst was fabricated and characterized as reported in our work [21]. In the second step of reducing Cu-Co/STO precursor, Cu species were dispersed on the original Co/STO surface. According to XRD analysis of Cu modified Co/STO after calcination, the peaks of the Co and Cu metal phases are broadened and the peak intensities are decreased (Fig. 1b), which indicates the smaller size and more uniformly dispersion of nanoparticles [27,28]. To further identify the elemental composition and chemical states of Cu-Co/STO catalyst, XPS analysis was carried out (Fig. 1c–d and Fig. S1). The XPS spectrum of Co 2p (Fig. 1c) shows the presence of metal Co^0 with a characteristic peak at 778.5 eV binding energy. The XPS spectrum of Cu 2p was also collected and shown in Fig. 1d. The peak with the binding energy of 932.4 eV can be attributed to the signal of Cu^0 [29]. Thus, the results revealed that Co and Cu nanoparticles on STO are maintained in the metallic state.

The microstructure of the Cu-Co/STO catalyst was illustrated in Fig. 2. TEM images show that the representing Cu and Co nanoparticles were loaded on STO support (Fig. 2a). The average diameter of these particles is 5.8 nm, and the nanoparticles sizes are mainly distributed in the range of 5–7 nm (insert of Fig. 2a). Fig. 2b–d and Fig. S2 show the three-component interface structure of Cu-Co/STO. A metal nanoparticles statistic of TEM images demonstrates that the distribution of adjacent nanoparticles is over 65% (Fig. S2). From HR-TEM images of 1.5Cu-2Co/STO, the adjacent Cu and Co nanoparticles uniformly distribute on the STO surface, which proves by the fact that Cu of low surface energy is enriched on the Co surface (Fig. 2b–d), and a similar material design concept has been confirmed by variable Mo loaded Ru/γ-Al_2O_3 nanoparticles [30]. According to EDS linear scan (Fig. S3), the three phase interface composed of neighboring Cu and Co nanoparticles loaded on STO is clearly discernible. The lattice fringes with a spacing of 0.205 and 0.208 nm can be assigned to the (111) planes of Co and Cu, respectively. As the loading amount of Cu increases, it is likely that the Co nanoparticles are partially covered. For the 5Cu-2Co/STO catalyst, Co is coated with Cu on the STO substrate (Fig. 2d and Fig. S4), which

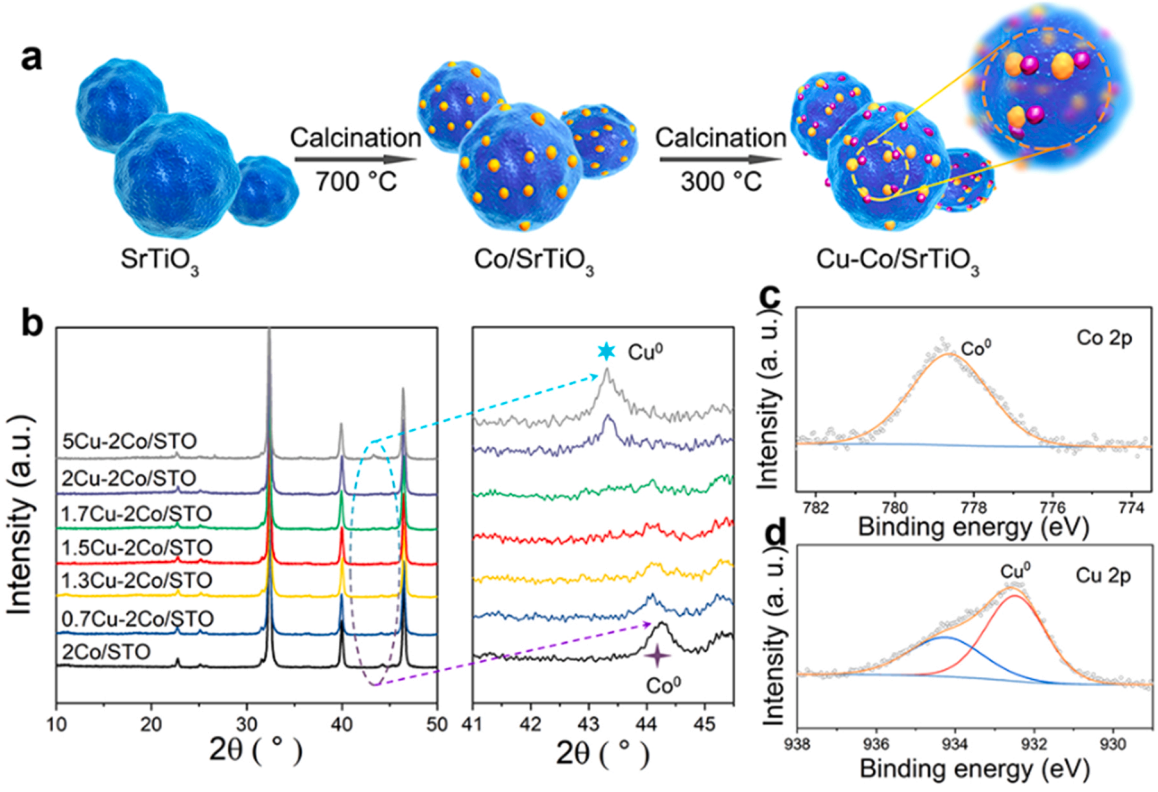

Fig. 1. (a) Schematic illustration of the two-step preparation process for the Cu-Co/STO catalysts. (b) The XRD pattern of the Cu-Co/STO catalysts. The XPS spectra of (c) Co 2p and (d) Cu 2p for 1.5Cu-2Co/STO.

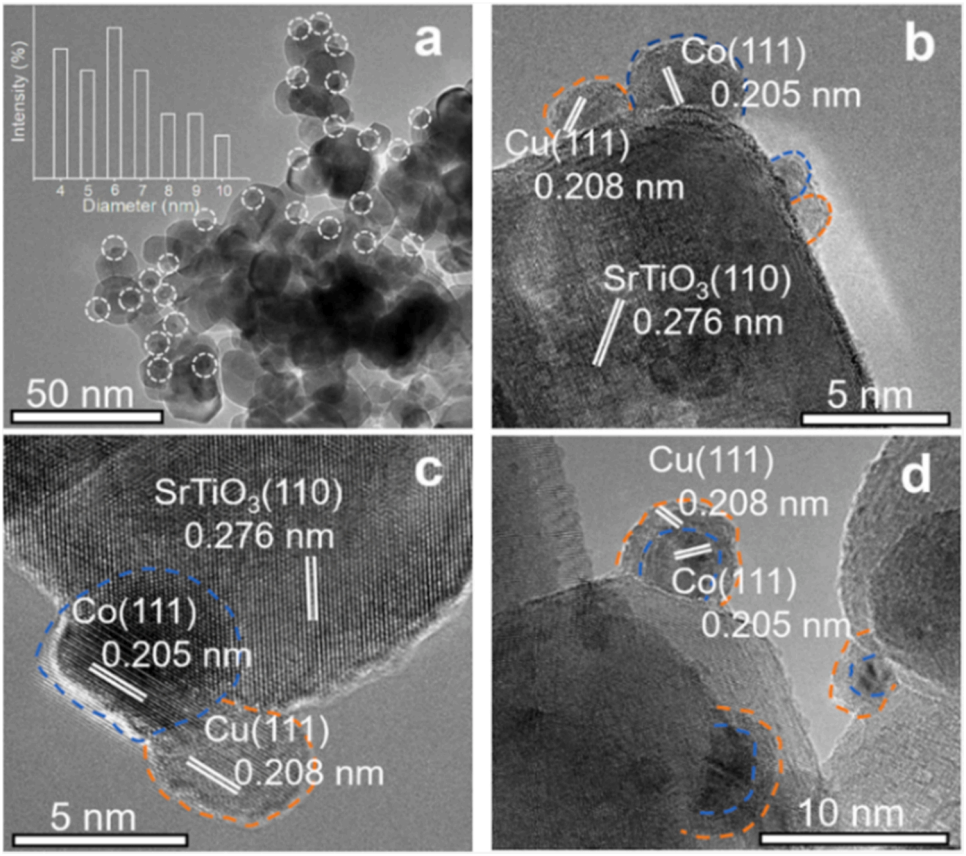

Fig. 2. (a) TEM and HR-TEM images of the (b, c) 1.5Cu-2Co/STO and (d) 5Cu-2Co/STO.

reduces the number of catalytic active sites. Thus, optimizing the loading of Cu and Co nanoparticles on STO to effectively expose the active sites is conducive to boosting catalytic performance.

3.2. Co and Cu co-loaded $SrTiO_3$ to enhance Fischer-Tropsch synthesis but to suppress water-gas shift reaction

Light absorption property and light-to-thermal conversion efficiency are the two important factors for efficient light-driven catalysis. The UV–visible-IR absorption spectra were conducted to study light absorption behavior (Fig. 3a and Fig. S5). All samples show an absorption edge at around 375 nm, which indicates that there is no doping effect of Co and Cu on changing the bandgap of STO. However, compared with STO, the light absorption of other as-prepared catalysts increase in the UV–visible-IR region of solar spectrum and equilibrium photothermal conversion temperature is promoted (Fig. 3b and Fig. S6); An increase of LSPR-Cu loading caused the high efficiency of light-to-thermal conversion as compared to the monometallic Co system (247 °C for 2Co/STO vs 290 °C for 1.5Cu-2Co/STO), and therefore, an enhanced photothermal effect was achieved over Cu-Co/STO catalyst to provide a higher local temperature to drive the surface catalysis.

In order to assess the synergistic effect of Cu and Co on catalytic efficiency under solar light irradiation, the CO conversion was carried out over the as-synthesized catalysts. As for 1.5Cu/STO (with 1.5 wt% of Cu loading), CO_2 selectivity is as high as 91.8% (Table S1), revealing the WGS reaction is dominant [31]; however, its activity is relatively low and TOC yield of the product is below 0.01 mmol g^{-1} h^{-1}. The H_2O molecules adsorbed on the surface of the catalyst and a small amount of H_2O generated by CO hydrogenation are the CO combustion adjuvant for this WGS reaction. The 2Co/STO catalyst presents the selectivity for value-added hydrocarbons (with 34.8% of C2–C4 hydrocarbons) but the CO_2 selectivity is up to 48.1%. Interestingly, Cu and Co co-loaded STO significantly increases the CO conversion, and the light-driven catalytic reaction path is changed from WGS to FTS. The 1.5Cu-2Co/STO catalyst exhibits optimal activity (Fig. 3d); in comparison with 2Co/STO and 1.5Cu/STO, the CO conversion is 26.4%, nearly 2- and 7-fold promotion (Fig. 3e), respectively, which can be mainly attributed to the fact that the co-loading of nano-metals improves the photothermal conversion efficiency and there is a synergistic effect between Cu and Co. Thus, due to the change of catalytic reaction path, the 1.5Cu-2Co/STO catalyst produces TOC of hydrocarbons with C2–C4 yield of 1.36 mmol g^{-1} h^{-1} by light-driven catalysis (Fig. 3e), and the selectivity of C2–C4 is up to 53.4% nearly 1.5- and 17-fold enhancement in comparison with that of 2Co/STO and 1.5Cu/STO, respectively. The FTS performance of the adjacent metals-structure of 1.5Cu-2Co/STO-PD obtained by the photo-deposition method is similar to that of 1.5Cu-2Co/STO. This result indicates that both ways successfully obtained adjacent Cu and Co loaded STO (Fig. 2 and Fig. S7), and show excellent light-induced enhanced photo- and thermal-synergistic-catalytic performance. However, the 1.5Cu-2Co/STO-300D and 1.5Cu-2Co/STO-700D catalysts synthesized in one-step calcination and reduction show low C2–C4 selectivity (Fig. 3e), which confirms that the alloy structure cannot show the characteristics of the photo-induced synergistic effect of neighboring nano-metals. However, under the identical operating conditions of external heating at 290 °C, the catalysts have low CO conversion performance (Fig. S8), and the CO_2 selectivity of the product is as high as 87.2%, 93.5% and 90.5% for 2Co/STO, 1.5Cu/STO, and 1.5Cu-2Co/STO, respectively. This indicates that the catalysts mainly engage in WGS reaction by thermal-driven catalysis. Furthermore, the effect of support on catalytic performance was explored. When the STO is substituted by SiO_2 (traditional insulator support), the C2–C4 yield of 1.5Cu-2Co/SiO_2 catalyst is far lower than that of 1.5Cu-2Co/STO (Table S1). Therefore, the interaction of the three components of Cu, Co and STO are essential to change the conversion path of CO and

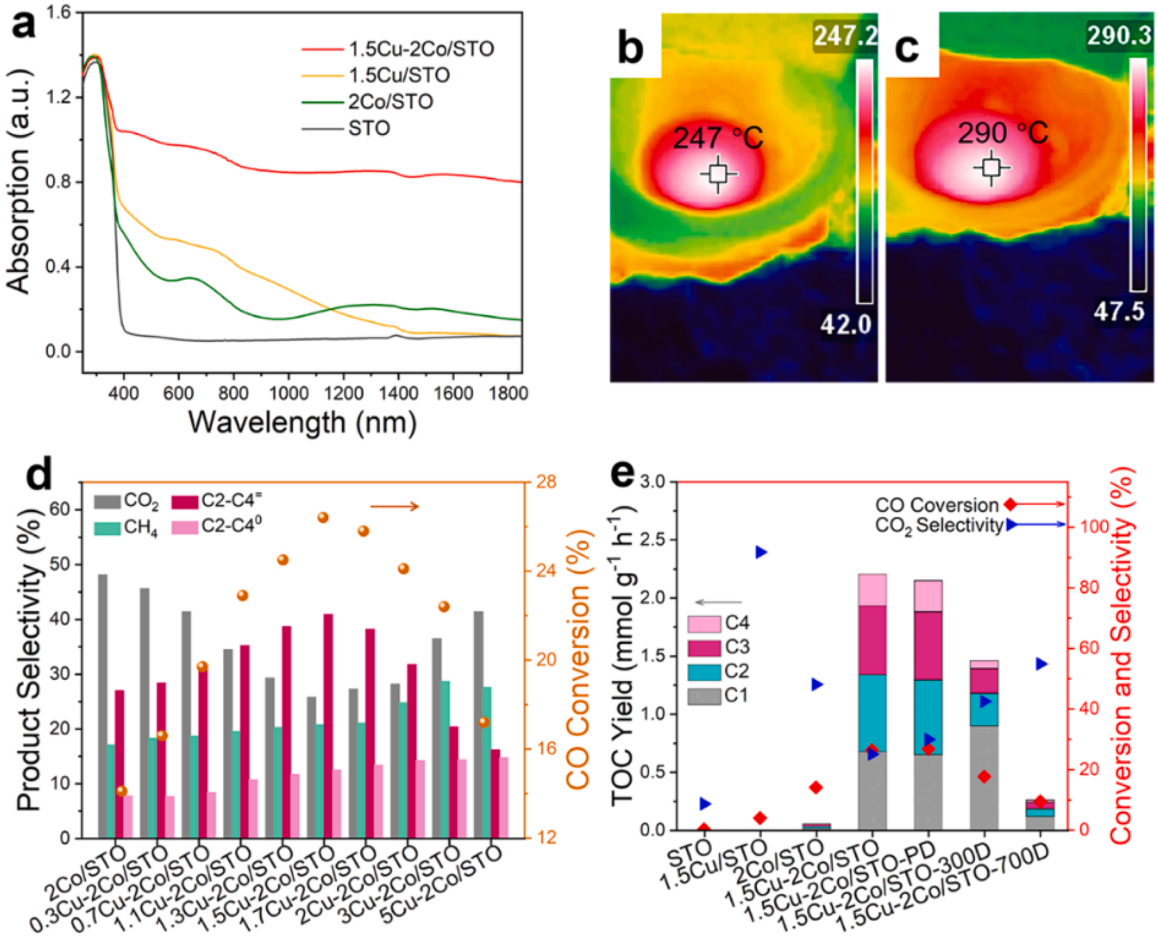

Fig. 3. (a) UV–visible-IR spectra of the as-prepared catalysts; 2D IR images of (b) 2Co/STO and (c) 1.5Cu-2Co/STO catalyst on a reactor under the illumination of 300 W Xe lamp; (d) The product selectivity and CO conversion over different xCu-2Co/STO catalysts under light irradiation; (e) The product yield calculated as TOC amount of C1–C4 hydrocarbons, the CO_2 selectivity and CO conversion.

improve the light-induced catalytic performance. To study the performance stability of the 1.5Cu-2Co/STO, recycling experiment of light-driven catalysis was carried out (Fig. S15). The catalyst shows smooth trends of CO conversion rate and C2–C4 selectivity, suggesting the stable catalytic performance of the Cu-Co/STO catalyst. Next, we study the catalytic mechanism of light-driven Cu-Co/STO to convert CO to C2–C4 hydrocarbons.

3.3. The mechanism of light-driven enhanced photo- and thermal-synergistic catalysis over Cu-Co/$SrTiO_3$ catalyst

3.3.1. Adsorption performance of active sites of catalysts for H_2 and CO

In general, for the Co- and Cu-based catalysts, Co^0 and Cu^0 are believed to be the sole active sites and primarily responsible for the activity of the catalyst [28,32]. Light-driven heating is beneficial for the in situ activation of catalysts in the reducing atmosphere. The H_2-TPR spectra show that the unstable species on the catalyst surface can be reduced in H_2 reduction atmosphere at low temperature (Fig. S9). The UV–visible-IR absorption spectra were applied to reveal the absorption peak of LSPR effect over Cu-Co/STO catalyst (Fig. S10). The activated catalyst obtained in above way was used for the following characterization. Fig. 4a illustrates H_2 adsorption on catalysts when the sample was reduced via the measurement of H_2-TPD. A contrast measurement of H_2-TPD over the STO support was conducted, and there are no signals for H_2 desorption, which could exclude the influence of the STO support on H_2 adsorption. The H_2 desorption of the 1.5Cu-2Co/STO at temperature ranges of 55–220 °C and 300–400 °C are respectively assigned to chemisorbed H species at the Co and Cu metallic state; the lower desorption temperature of Co-H than that of Cu-H reveals that the H on the surface of Co is easy to be dissociated, and therefore, it can be inferred that Co is the active site for H_2 activation. Moreover, the desorption temperature of Co-H in 1.5Cu-2Co/STO is significantly decreased in comparison with that in 2Co/STO, which is probably caused by the Cu closely contacting with Co to affect its surface property. According to a study of the CO-TPD (Fig. 4b), a contrast measurement of CO-TPD over the STO support was conducted, and there is no clear CO adsorption signal. Compared to 1.5Cu/STO, two strong peaks which are respectively located in the low-temperature range of 90–250 °C and the high-temperature range of 320–480 °C are observed for both the 2Co/STO and 1.5Cu-2Co/STO catalysts, which suggests that the CO molecules are predominantly adsorbed on the Co species. Moreover, in contrast with the convolution of the curves of 2Co/STO and 1.5Cu/STO (Fig. S11), the temperature range of 170–250 °C of CO desorption over 1.5Cu-2Co/STO are assigned to chemisorbed CO at the interface of Cu and Co, which lends support to the neighbored location of Cu and Co nanoparticles. Next, we characterized the surface of 1.5Cu-2Co/STO nanoparticles by DRIFTS experiment following CO adsorption. The 1.5Cu-2Co/STO generated distinct peaks assignable to the Co and Cu linear stretching vibrations of adsorbed CO at 2176, 2116 and 2106 cm^{-1} (Fig. 4c), respectively. The 2Co/STO show two apparent absorption peaks at 2176 and 2116 cm^{-1} on the bottom and top of the doublet for gas-phase CO. As for 1.5Cu/STO, the band of linearly adsorbed CO at 2106 cm^{-1} remains rather narrow [33]. The 1.5Cu/STO has a weak adsorption capacity for CO than 2Co/STO, and meanwhile,

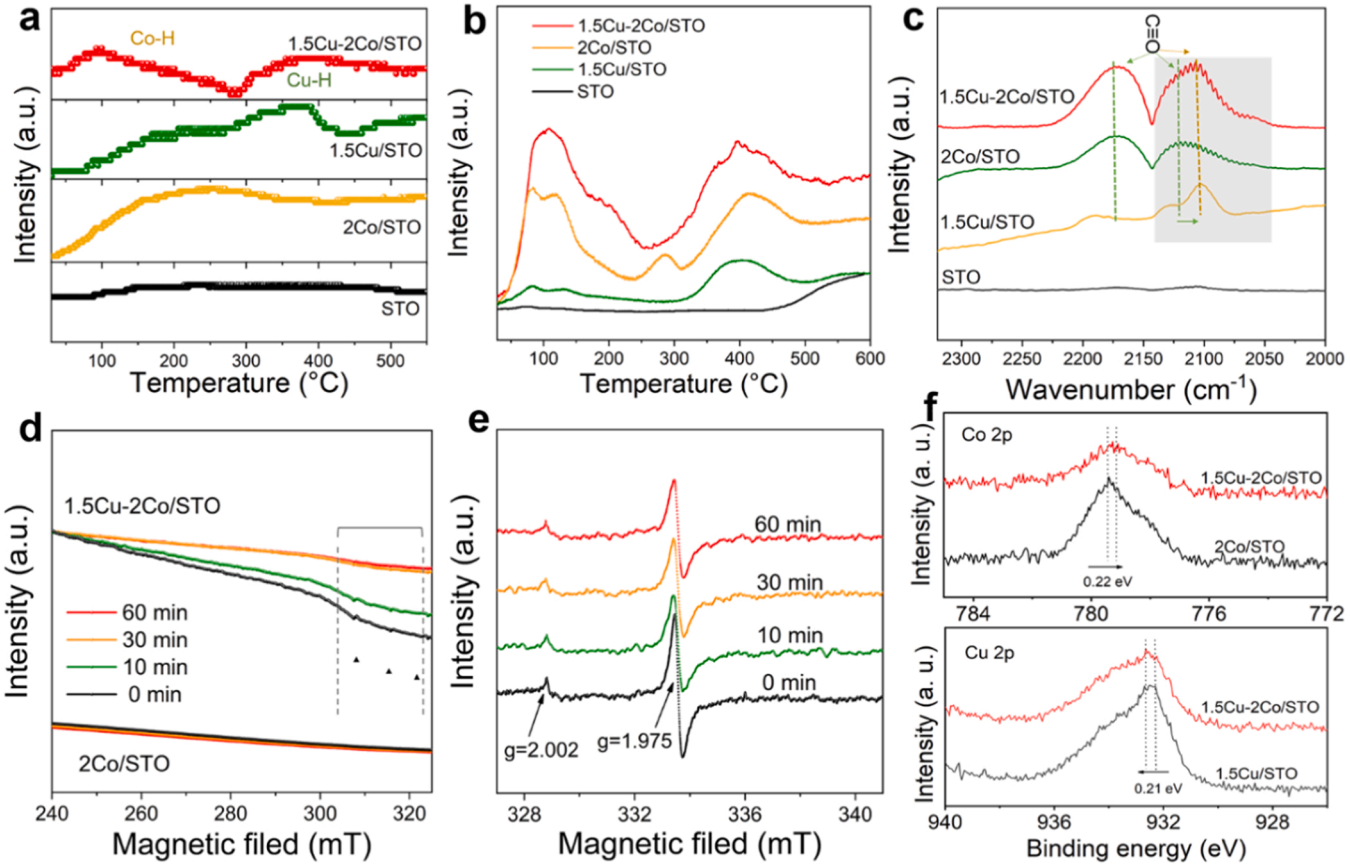

Fig. 4. Comparison of H_2-TPD profiles (a), CO-TPD profiles (b) and DRIFTS spectra of CO chemisorbed on catalyst surface (c) of 1.5Cu/STO, 2Co/STO, and 1.5Cu-2Co/STO catalysts. The ESR spectra of 2Co/STO (d) and 1.5Cu-2Co/STO (d and e) under light illumination. (f) The XPS spectra of different catalysts: Co 2p and Cu 2p.

the profile of the curve of 1.5Cu-2Co/STO is similar to that of 2Co/STO, which indicates that Co species are the predominant-adsorption sites for CO and is consistent with the results of CO-TPD. Since the absorption range of 1.5Cu/STO is mainly located at 2075–2150 cm^{-1}, a detailed comparison between the curve of 1.5Cu-2Co/STO and the convolution of the curves of 2Co/STO and 1.5Cu/STO at this region were carried out; their profiles present different (Fig. S12), which again reveals the formation of adjacent structure of Cu and Co nanoparticles.

3.3.2. *Light-induced photo- and thermal-chemical property of Cu-Co/$SrTiO_3$*

To study the transfer of electrons induced by photocatalysis, we carried out the characterizations of ESR, XPS and DRIFTS over Cu-Co/$SrTiO_3$. The measurement of ESR under light irradiation (Figs. 4d and 4e) was adopted to investigate the light-induced photocarriers property of catalysts with different reaction time. As shown in Fig. 4d, compared with the unchanged spectra of 2Co/STO, the peak intensity of 1.5Cu-2Co/STO is weakened within the 60 min of the reaction, which is due to the activation of diamagnetic Cu^+/Cu^0 ($g = 2.32$) and Co^0 ($g = 2.20$–2.29) by light-induced photocarriers [34–36]. During the reaction progress, a small reduced signal appears at $g = 2.002$, which is attributable to trapped holes; the signal of trapped electrons at $g = 1.975$ shows a decrease tendency with the light irradiation (Fig. 4e). Thus, the signal that assigns for trapped holes and electrons in Cu-Co/STO photocatalyst are observed, revealing the photocatalytic effect over Cu-Co/STO catalyst. In addition, the study of photocurrent and photoluminescence also show the photocarriers separation and transfer over Cu-Co/STO (Figs. S13 and S14). However, what is the transfer direction of light-induced electrons at the interface among Cu, Co and STO? As exhibited in XPS results, the Co 2p peak of 1.5Cu-2Co/STO sample is shifted to lower binding energy than that of the 2Co/STO (Fig. 4f); conversely, compared to 1.5Cu/STO sample, the Cu 2p peak of 1.5Cu-2Co/STO moves to higher binding energy. The opposite XPS binding-energy shifts of the Cu and Co of 1.5Cu-2Co/STO indicate the electrons transfer from the Cu to the Co, which once more manifests the adjoining of Cu and Co nanoparticles. It can be explained that the increased electron density around Co is due to the introduction of Cu species, directly indicating that the charge flows to the surface Co atoms, which is similar to previously reported results of Ru and Cu nanoparticles co-dispersed on graphene [37]. Furthermore, back to the DRIFTS results, it can be observed that the main peak of CO desorption (at 2106 cm^{-1}) over 1.5Cu-2Co/STO is gradually shifted to lower wavenumber compared with the peak of 2Co/STO at 2116 cm^{-1} (Fig. 4c), which infers the interaction of the interface of Cu and Co in 1.5Cu-2Co/STO. This is also explained that the electronic shift can occur on the Co surface from Cu, resulting in a change of the adsorption property of the Co, which is in keeping with previous studies [38,39]. Theoretically, due to the difference in the net ionization potential between the two metals in Cu-Co/STO (Co: 7.86 eV, Cu: 7.73 eV) [39], the charge transfer of Cu atoms promotes the evident enrichment of electrons in Co atoms. All these results demonstrate that the synergy of Cu, Co and STO can enhance the generation and transport of light-induced injection of hot electrons and photocarriers, thus rendering high efficiency of CO reduction.

Some contrast experiments of catalytic performance evaluation over the 1.5Cu-2Co/STO were designed to further reveal the synergistically enhanced effect of injection of hot electrons and photocarriers (Fig. 5a). In the tests of the thermocatalysis (abbreviated as TC) and the solar-driven catalysis (SC), the reaction temperatures were fixed to be 290 °C; for executing an individual photocatalysis, the most of IR light

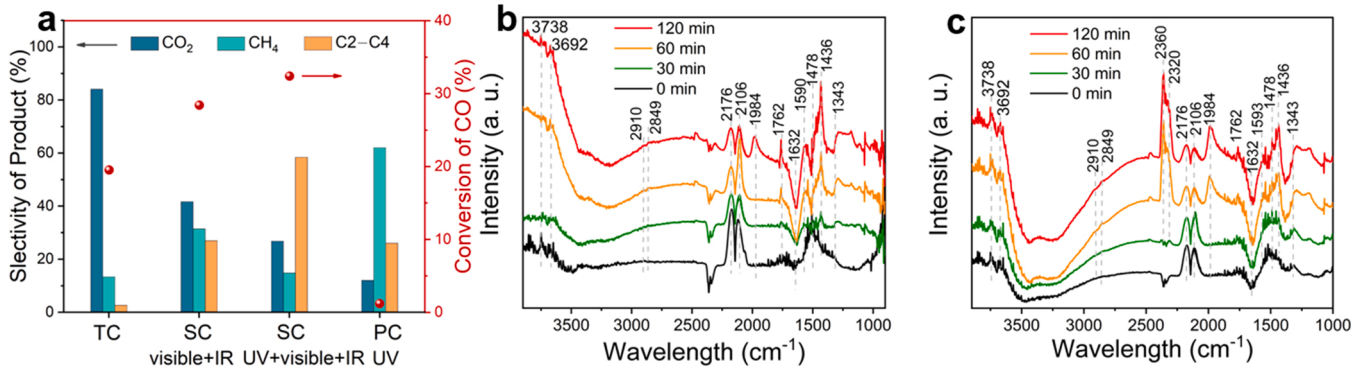

Fig. 5. (a) The CO conversion and product selectivity of the 1.5Cu-2Co/STO catalyst via thermal energy at 290 °C (TC: thermocatalysis) and solar energy (SC: solar-driven catalysis (visible-IR), ~ 288 °C; SC: UV–visible-IR light, ~ 290 °C; PC: photocatalysis (UV light, ~ 60 °C). The DRIFTS spectra of the adsorbed and convertible species of 1.5Cu-2Co/STO catalysts with (b) the coordinated effect of light and heat (290 °C), and thermal energy at 290 °C (c, thermocatalysis).

was excluded by an aggregate unit of water-cooling window, and thus, the reaction temperature was only 60 °C. In the individual thermocatalysis, the WGS reaction was dominant, and the CO_2 occupied the ~ 90.5% of product selectivity (Fig. 5a); this result can be ascribed to that the Cu or Co nanoparticles induced the WGS reaction. Under the SC with visible-IR irradiation, the hot electrons of Cu were excited. The thermal effect from the quenching of hot electrons could be excluded since the reaction temperature was fixed; therefore, the effect of the transferred hot electrons from Cu to Co can be well exhibited. These hot electrons activated the CO adsorbed over Co and thus the FTS occurred, which caused that the main product became C1–C4 hydrocarbons with a majority product as CH_4 and the selectivity of CO_2 was significantly reduced. In contrast, when the full-spectral SC (under irradiation of UV–visible-IR light) was evaluated, the yield of C1–C4 organics further increased, and C2–C4 obviously exceeded that of CO_2. More importantly, the selectivity for C2–C4 hydrocarbons was far higher than that for CH_4, indicating the high-energy photogenerated and hot electrons were easy to participate the C-C coupling process. The light-induced injection of hot electrons and photocarriers for synergistically enhanced photothermocatalysis of FTS delivered high catalytic efficiency towards value-added chemicals. As to the individual photocatalysis, the CH_4 was the predominant product; therefore, at low reaction temperature, the high-energy photoelectrons main drove the formation of C1 compound. This group of contrast experiments clearly reveal that the injection of hot electrons, photocarriers and heat are essential to generate value-added C2–C4 hydrocarbons.

Moreover, we gain insight into the effects of light and thermal on the pathway of CO conversion by employing in situ DRIFTS measurements (Figs. 5b and 5c). After successive adsorption in dark for 30 min, the spectrums of the sample were recorded and this time was defined as 0 min. Then, after H_2 was introduced into the reaction chamber, the cooperative light- and thermal-driven test used to simulate the former light-driven activity evaluation was started. The spectra were recorded at 30, 60 and 120 min, respectively (Fig. 5b). The band of CO adsorption at 2176 cm^{-1} decreases and the intensity of 2106 cm^{-1} increases gradually as the reaction proceeds, and the bridge adsorption at ~ 1984 cm^{-1} enhances progressively, which is due to the CO adsorption-induced surface reconstruction [40,41]. For the cooperative light- and thermal-driven catalysis from 30 to 120 min reaction (Fig. 5b), an additional band at 1762 cm^{-1} appears and can be ascribed to COH* species which is identified as reaction intermediates in the activated hydrogen reaction pathway for CO hydrogenation [21,42]; the characteristic asymmetric, symmetric υ(CH) vibrations and bending δ(CH) signals of intermediate of methylene (CH_2) groups are observed at 2910, 2849 and 1436 cm^{-1} [43], respectively; their intensities increase with reaction time prolonging, which indicates the formation of C2–C4 hydrocarbons. After the completion of cooperative light- and thermal-driven experiment, the chamber was vacuumized and then was re-fed with fresh catalyst and re-introduced with gaseous reactants; followed that, the thermal-driven measurement was executed. As exhibited in Fig. 5c, the surface formate species from reduction of bicarbonates (the bands at 1478 cm^{-1}) was presented by the OCO mode at 1593 cm^{-1} υ_{as} (OCO) and 1343 cm^{-1} υ_s (OCO) (Fig. 5c), are observed [44], Formation of HOCO* species is key evidence for the WGS reaction. After 30-min reaction, obviously, multiple positive peaks are increased in the 3500–3750 cm^{-1} range and a negative peak at 1632 cm^{-1} is decreased (Fig. 5c), respectively, corresponding to the absorption of OH groups formed and H_2O self-consumption [45]; two bands of CO_2 molecule with high peak intensity at 2360 cm^{-1} and 2320 cm^{-1} increase gradually. The evolution of these intermediates also lends support to the undergoing of the WGS reaction. Therefore, the thermal-driven catalysis is conducive to the WGS reaction to generate CO_2, while the full spectrum light-driven catalysis is beneficial for the FTS to produce C2–C4 hydrocarbons.

3.3.3. *Probable catalytic pathways for Cu-Co/$SrTiO_3$ catalyst*

The mechanism of the CO conversion over Cu-Co/$SrTiO_3$ catalyst was depicted in Fig. 6. The CO adsorption is verified to predominantly occur on Co, which is facilitated by the interaction of Co and Cu (correspondence well with the CO-TPD and DRIFTS results in Figs. 4b and 4c). For thermal-driven WGS reaction over Cu-Co/STO (Fig. 6a), the Cu and Co provide the active sites for CO chemisorption and make it to be oxidized to CO_2 through the form of HOCO* intermediates (it is confirmed well by in situ DRIFTS by thermal-driven experiment in Fig. 5c). Oxygen vacancies are formed at the interface of metal and oxide of Cu-Co/STO during the WGS process; they serve as active site to dissociate O from adsorbed H_2O and then oxidize CO into CO_2 [31,46]. Solar light-excited photocarriers and injection of hot electrons (Fig. 6b) are considered to be the driving force for the induced photo- and thermal-synergy to promote FTS over Cu-Co/STO catalyst. For light-induced photogenerated carriers, theoretically, Co has a higher work function (~ 5.0 eV) [47] compared with the work function of $SrTiO_3$ (~ 4.4 eV) [48] and Cu (~ 4.8 eV) [49], and therefore can be used as electrons accumulator (corroborating with the DRIFTS, ESR and XPS experiments in Fig. 4c–f). Due to the excitation of STO support and LSPR-active Cu nanoparticles by UV–visible-IR light, their photoelectrons and active hot electrons can migrate toward active phase of Co. For photothermal effect, the neighbored Cu and Co nanoparticles have a synergistic effect of light-to-thermal conversion and the excited hot electrons with poor mobility tend to be quenched to produce heat (it was verified by temperature monitoring experiments of catalysts in Fig. 3b–c). The Cu and Co synergistically promote the activation of the adsorbed H_2 and CO molecules (which was demonstrated by H_2-TPD, CO-TPD and DRIFTS in Fig. 4a–c). We concluded that the FTS is driven by light-induced injection of hot electrons and photocarriers for synergistically enhanced photothermocatalysis over Co-Cu/STO under full

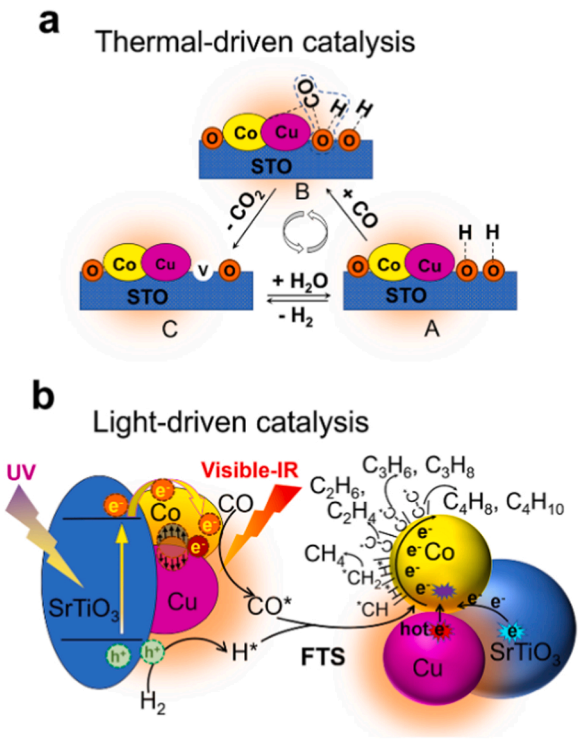

Fig. 6. (a) Schematic illustration of thermocatalysis of WGS reaction over Cu-Co/STO; (b) The effect of light-induced injection of hot electrons and photocarriers for synergistically enhanced photothermocatalysis of FTS reaction over Cu-Co/STO.

spectrum irradiation (Fig. 6b). The Co nanoparticles accumulate the photogenerated/hot electrons and heat to drive CO hydrogenation, and photoholes enhance to activate hydrogen, which are beneficial to form COH*(CH_2*) intermediate species (which corroborates well via in situ DRIFTS by coupled light- and thermal-driven experiment in Fig. 5b), and thus promotes the C-C coupling towards a enhanced high selectivity for C2–C4 hydrocarbons.

4. Conclusion

In summary, we demonstrate that a light-induced photo- and thermal-synergistic catalysis can be constructed via co-loading neighbored Co and Cu over $SrTiO_3$ semiconductor. The $SrTiO_3$, Co and Cu serve as sensitizers to sufficiently absorb and effectively convert the full-spectral solar light, which couples the photocatalytic and photothermal effects to drive the subsequent catalytic process. In comparison with the individual photocatalysis and thermocatalysis over Cu-Co/$SrTiO_3$ to undergo CO methanation and water-gas shift reaction, respectively, the light-induced enhanced photo- and thermal-synergistic catalysis can achieve superior CO conversion as Fischer-Tropsch synthesis. The optimal performance was achieved over 1.5Cu-2Co/STO which exhibited high activity in the CO hydrogenation to C2–C4 hydrocarbons with a TOC evolution rate of 1.36 mmol g^{-1} h^{-1}, and the selectivity of C2–C4 reached 53.4% which was nearly 1.5- and 17.2-fold enhancement compared with 2Co/STO and 1.5Cu/STO, respectively. The microstructural configuration of neighbored nano-metals (Cu and Co nanoparticles) co-loading on semiconductor ($SrTiO_3$) provides a fluent route for active component to accumulate the light-induced electrons and heat, which is vital for the system of light-induced injection of hot electrons and photocarriers for synergistically enhanced photothermocatalysis; thus, the microstructural architecture of catalyst is worth to be further explored and optimized. This work provides a new perspective toward light-induced energy-efficient heterogeneous catalysis and related sustainable energy conversion systems.

CRediT authorship contribution statement

Shangbo Ning: Investigation, Software, Writing – original draft. **Yanhui Sun:** Software, Methodology. **Shuxin Ouyang:** Project administration, Supervision, Writing – review & editing, Funding acquisition. **Yuhang Qi:** Methodology, Formal analysis. **Jinhua Ye:** Writing – review & editing, Supervision, Funding acquisition.

Declaration of Competing Interest

The authors declare that they have no known competing financial interests or personal relationships that could have appeared to influence the work reported in this paper.

Acknowledgements

This work received financial support from the National Natural Science Foundation of China (Grants 21972052 and 21633004) and JSPS KAKENHI of Japan (Grant no. JP18H02065).

Appendix A. Supplementary material

Additional experimental date: Additional data for characterization (e.g., chemicals and materials, characterization of catalysts, Figs. S1–S15 and Table S1).

Appendix B. Supporting information

Supplementary data associated with this article can be found in the online version at doi:10.1016/j.apcatb.2022.121063.

References

[1] Q.S. Ruan, T.N. Miao, H. Wang, J.W. Tang, Insight on shallow trap states-introduced photocathodic performance in n-type polymer photocatalysts, J. Am. Chem. Soc. 142 (2020) 18277–18278.
[2] G.B. Chen, G.I.N. Waterhouse, R. Shi, J.Q. Zhao, Z.H. Li, L.Z. Wu, C.H. Tung, T. R. Zhang, From solar energy to fuels: recent advances in light-driven C1 chemistry, Angew. Chem. Int. Ed. 58 (2019) 17528–17551.
[3] L.H. Lin, Z.Y. Lin, J. Zhang, X. Cai, W. Lin, Z.Y. Yu, X.C. Wang, Molecular-level insights on the reactive facet of carbon nitride single crystals photocatalysing overall water splitting, Nat. Catal. 3 (2020) 649–655.
[4] M.M. Hao, Y. Bai, S. Zeiske, L. Ren, J.X. Liu, Y.B. Yuan, N. Zarrabi, N.Y. Cheng, M. Ghasemi, P. Chen, M.Q. Lyu, D.X. He, J.H. Yun, Y. Du, Y. Wang, S.S. Ding, A. Armin, P. Meredith, G. Liu, H.M. Cheng, L.Z. Wang, Ligand-assisted cation-exchange engineering for high-efficiency colloidal $Cs_{1-x}FA_xPbI_3$ quantum dot solar cells with reduced phase segregation, Nat. Energy 5 (2020) 79–88.
[5] M. Gratzel, Photoelectrochemical cells, Nature 414 (2001) 338–344.
[6] J. Li, L.J. Cai, J. Shang, Y. Yu, L.Z. Zhang, Giant enhancement of internal electric field boosting bulk charge separation for photocatalysis, Adv. Mater. 28 (2016) 4059–4064.
[7] Y. An, Y.Y. Liu, P.F. An, J.C. Dong, B.Y. Xu, Y. Dai, X.Y. Qin, X.Y. Zhang, M. H. Whangbo, B.B. Huang, Ni-II coordination to an Al-based metal-organic framework made from 2-aminoterephthalate for photocatalytic overall water splitting, Angew. Chem. Int. Ed. 56 (2017) 3036–3040.
[8] Z. Zou, J. Ye, K. Sayama, H. Arakawa, Direct splitting of water under visible light irradiation with an oxide semiconductor photocatalyst, Nature 414 (2001) 625–627.
[9] S. Ouyang, H. Tong, N. Umezawa, J. Cao, P. Li, Y. Bi, Y. Zhang, J. Ye, Surface-alkalinization-induced enhancement of photocatalytic H_2 evolution over $SrTiO_3$-based photocatalysts, J. Am. Chem. Soc. 134 (2012) 1974–1977.
[10] Y.G. Zhou, Y.F. Zhang, M.S. Lin, J.L. Long, Z.Z. Zhang, H.X. Lin, J.C.S. Wu, X. X. Wang, Monolayered Bi_2WO_6 nanosheets mimicking heterojunction interface with open surfaces for photocatalysis, Nat. Commun. 6 (2015) 1–8.
[11] J. Li, X.Y. Wu, W.F. Pan, G.K. Zhang, H. Chen, Vacancy-rich monolayer BiO_{2-x} as a highly efficient UV, Visible, and near-Infrared responsive photocatalyst, Angew. Chem. Int. Ed. 57 (2018) 491–495.
[12] Q. Zhang, X.M. Liu, L. Tan, Z.D. Cui, X.J. Yang, Z.Y. Li, Y.Q. Liang, S.L. Zhu, K.W. K. Yeung, X.B. Wang, Y.F. Zheng, S.L. Wu, A near infrared-activated photocatalyst based on elemental phosphorus by chemical vapor deposition, Appl. Catal. B-Environ. 258 (2019), 117980.
[13] Z.H. Li, J.J. Liu, Y.F. Zhao, G.I.N. Waterhouse, G.B. Chen, R. Shi, X. Zhang, X. W. Liu, Y.M. Wei, X.D. Wen, L.Z. Wu, C.H. Tung, T.R. Zhang, Co-based catalysts derived from layered-double-hydroxide nanosheets for the photothermal production of light olefins, Adv. Mater. 30 (2018), 1800527.

[14] M. Tou, R. Michalsky, A. Steinfeld, Solar-driven thermochemical splitting of CO_2 and in situ separation of CO and O_2 across a ceria redox membrane reactor, Joule 1 (2017) 146–154.
[15] T.J. Yan, L. Wang, Y. Liang, M. Makaremi, T.E. Wood, Y. Dai, B.B. Huang, A. A. Jelle, Y. Dong, G.A. Ozin, Polymorph selection towards photocatalytic gaseous CO_2 hydrogenation, Nat. Commun. 10 (2019) 1–10.
[16] G. Wang, B. Huang, X. Ma, Z. Wang, X. Qin, X. Zhang, Y. Dai, M.H. Whangbo, $Cu_2(OH)PO_4$, a near-infrared-activated photocatalyst, Angew. Chem. Int. Ed. 52 (2013) 4810–4813.
[17] Y. Sang, Z. Zhao, M. Zhao, P. Hao, Y. Leng, H. Liu, From UV to near-infrared, WS2 nanosheet: a novel photocatalyst for full solar light spectrum photodegradation, Adv. Mater. 27 (2015) 363–369.
[18] X.G. Meng, T. Wang, L.Q. Liu, S.X. Ouyang, P. Li, H.L. Hu, T. Kako, H. Iwai, A. Tanaka, J.H. Ye, Photothermal conversion of CO_2 into CH_4 with H_2 over group VIII nanocatalysts: an alternative approach for solar fuel production, Angew. Chem. Int. Ed. 53 (2014) 11478–11482.
[19] S.B. Ning, H. Xu, Y.H. Qi, L.Z. Song, Q.Q. Zhang, S.X. Ouyang, J.H. Ye, Microstructure induced thermodynamic and kinetic modulation to enhance CO_2 photothermal reduction: a case of atomic-scale dispersed Co-N species anchored Co@C hybrid, ACS Catal. 10 (2020) 4726–4736.
[20] Y.S. Wang, Y.F. Zhao, J.J. Liu, Z.H. Li, G.I.N. Waterhouse, R. Shi, X.D. Wen, T. R. Zhang, Manganese oxide modified nickel catalysts for photothermal CO hydrogenation to light olefins, Adv. Energy Mater. 10 (2020), 1902860.
[21] S. Ning, S. Wang, S. Ouyang, Y. Qi, X. Yi, H. Hu, J. Ye, Photocarriers-assisted photothermocatalysis of Fischer-Tropsch synthesis for enhanced yield of C2–C4 hydrocarbons over Co/$SrTiO_3$ catalyst, Catal. Sci. Technol. 11 (2021) 7029–7034.
[22] L. Collado, A. Reynal, F. Fresno, M. Barawi, C. Escudero, V. Perez-Dieste, J. M. Coronado, D.P. Serrano, J.R. Durrant, V.A.D. O'Shea, Unravelling the effect of charge dynamics at the plasmonic metal/semiconductor interface for CO_2 photoreduction, Nat. Commun. 9 (2018) 1–10.
[23] S. Jin, G.H. Dong, J.M. Luo, F.Y. Ma, C.Y. Wang, Improved photocatalytic NO removal activity of $SrTiO_3$ by using $SrCO_3$ as a new co-catalyst, Appl. Catal. B-Environ. 227 (2018) 24–34.
[24] S.G.Y. Weng, L. Wang, H. Lu, X. Meng, G.I.N. Waterhouse, S. Zhou, Defective porous carbon polyhedra decorated with copper nanoparticles for enhanced NIR-driven photothermal cancer therapy, Small 16 (2019), 1905184.
[25] L.Q. Liu, X.N. Zhang, L.F. Yang, L.T. Ren, D.F. Wang, J.H. Ye, Metal nanoparticles induced photocatalysis, Natl. Sci. Rev. 4 (2017) 761–780.
[26] Q.P. Cheng, S. Lyu, N. Zhao, K. Ma, T. Ding, Z. Jiang, L. Wang, J. Zhang, L. Zheng, F. Gao, L. Dong, N. Tsubaki, X. Li, Confined small-sized cobalt catalysts stimulate carbon-chain growth reversely by modifying ASF law of Fischer-Tropsch synthesis, Nat. Commun. 9 (2018) 1–9.
[27] H.P.R. Kannapu, Y.-W. Suh, V. Vaddeboina, A. Narani, D.R. Burri, S.R.R. Kamaraju, Nano CoO-Cu-MgO catalyst for vapor phase simultaneous synthesis of ortho-chloroaniline and γ-butyrolactone from ortho-cholonitrobenzne and 1,4-butane-diol, Character, Appl. Nanomater. 4 (2021) 1–9.
[28] S. Lyu, L. Wang, J. Zhang, C. Liu, J. Sun, B. Peng, Y. Wang, K.G. Rappé, Y. Zhang, J. Li, L. Nie, Role of active phase in Fischer-Tropsch synthesis: experimental evidence of CO activation over single-phase cobalt catalysts, ACS Catal. 8 (2018) 7787–7798.
[29] M.Y. Wang, L. Sun, Z.Q. Lin, J.H. Cai, K.P. Xie, C.J. Lin, p-n heterojunction photoelectrodes composed of Cu_2O-loaded TiO_2 nanotube arrays with enhanced photoelectrochemical and photoelectrocatalytic activities, Energ, Environ. Sci. 6 (2013) 1211–1220.
[30] K. Adamska, J. Okal, W. Tylus, Stable bimetallic Ru-Mo/Al_2O_3 catalysts for the light alkane combustion: effect of the Mo addition, Appl. Catal. B-Environ. 246 (2019) 180–194.
[31] J.L. Santos, T.R. Reina, S. Ivanova, M.A. Centeno, J.A. Odriozola, Gold promoted Cu/ZnO/Al_2O_3 catalysts prepared from hydrotalcite precursors: advanced materials for the WGS reaction, Appl. Catal. B-Environ. 201 (2017) 310–317.
[32] J. Gong, H. Yue, Y. Zhao, S. Zhao, L. Zhao, J. Lv, S. Wang, X. Ma, Synthesis of ethanol via syngas on Cu/SiO_2 catalysts with balanced Cu^0-Cu^+ sites, J. Am. Chem. Soc. 134 (2012) 13922–13925.
[33] C. Daniel, M.O. Clarte, S.P. Teh, O. Thinon, H. Provendier, A.C. Van Veen, B. J. Beccard, Y. Schuurman, C. Mirodatos, Spatially resolved catalysis in microstructured reactors by IR spectroscopy: CO oxidation over mono- and bifunctional Pt catalysts, J. Catal. 272 (2010) 55–64.
[34] L. Yuan, S.F. Hung, Z.R. Tang, H.M. Chen, Y.J. Xiong, Y.J. Xu, Dynamic evolution of atomically dispersed Cu species for CO_2 photoreduction to solar fuels, ACS Catal. 9 (2019) 4824–4833.
[35] D.A. Wheeler, J.Z. Zhang, Exciton dynamics in semiconductor nanocrystals, Adv. Mater. 25 (2013) 2878–2896.
[36] Y. Nosaka, S. Takahashi, H. Sakamoto, A.Y. Nosaka, Reaction mechanism of Cu(II)-grafted visible-light responsive TiO_2 and WO_3 photocatalysts studied by means of ESR spectroscopy and chemiluminescence photometry, J. Phys. Chem. C 115 (2011) 21283–21290.
[37] Z. Zhang, C. Yang, S.S. Wu, A.N. Wang, L.L. Zhao, D.D. Zhai, B. Ren, K.Z. Cao, Z. Zhou, Exploiting synergistic effect by integrating ruthenium-copper nanoparticles highly Co-dispersed on graphene as efficient air cathodes for Li-CO_2 batteries, Adv. Energy Mater. 9 (2019), 1802805.
[38] D. Song, J. Li, Q. Cai, In situ diffuse reflectance FTIR study of CO adsorbed on a cobalt catalyst supported by silica with different pore sizes, J. Phys. Chem. C 111 (2007) 18970–18979.
[39] K. Mori, T. Sano, H. Kobayashi, H. Yamashita, Surface engineering of a supported PdAg catalyst for hydrogenation of CO_2 to formic acid: elucidating the active Pd atoms in alloy nanoparticles, J. Am. Chem. Soc. 140 (2018) 8902–8909.
[40] M. Xu, S.Y. Yao, D.M. Rao, Y.M. Niu, N. Liu, M. Peng, P. Zhai, Y. Man, L.R. Zheng, B. Wang, B.S. Zhang, D. Ma, M. Wei, Insights into interfacial synergistic catalysis over Ni@TiO_{2-x} catalyst toward water-gas shift reaction, J. Am. Chem. Soc. 140 (2018) 11241–11251.
[41] T. Avanesian, S. Dai, M.J. Kale, G.W. Graham, X.Q. Pan, P. Christopher, Quantitative and atomic-scale view of CO-induced Pt nanoparticle surface reconstruction at saturation coverage via DFT calculations coupled with in situ TEM and IR, J. Am. Chem. Soc. 139 (2017) 4551–4558.
[42] S. Eckle, H.G. Anfang, R.J. Behm, Reaction intermediates and side products in the methanation of CO and CO_2 over supported Ru catalysts in H_2-rich reformate gases, J. Phys. Chem. C 115 (2011) 1361–1367.
[43] J. Schweicher, A. Bundhoo, A. Frennet, N. Kruse, H. Daly, F.C. Meunier, DRIFTS/MS studies during chemical transients and SSITKA of the CO/H_2 reaction over Co-MgO catalysts, J. Phys. Chem. C 114 (2010) 2248–2255.
[44] F. Polo-Garzon, V. Fung, L. Nguyen, Y. Tang, F. Tao, Y. Cheng, L.L. Daemen, A. J. Ramirez-Cuesta, G.S. Foo, M. Zhu, I.E. Wachs, D.E. Jiang, Z. Wu, Elucidation of the reaction mechanism for high-temperature water gas shift over an industrial-type copper-chromium-iron oxide catalyst, J. Am. Chem. Soc. 141 (2019) 7990–7999.
[45] Y. He, F. Guo, K.R. Yang, J.A. Heinlein, S.M. Bamonte, J.J. Fee, S. Hu, S.L. Suib, G. L. Haller, V.S. Batista, L.D. Pfefferle, In situ identification of reaction intermediates and mechanistic understandings of methane oxidation over hematite: a combined experimental and theoretical study, J. Am. Chem. Soc. 142 (2020) 17119–17130.
[46] J.J. Plata, J. Graciani, J. Evans, J.A. Rodriguez, J.F. Sanz, Cu deposited on CeO_x-modified TiO_2(110): synergistic effects at the metal-oxide interface and the mechanism of the WGS reaction, ACS Catal. 6 (2016) 4608–4615.
[47] Y. Inoue, M. Kitano, M. Tokunari, T. Taniguchi, K. Ooya, H. Abe, Y. Niwa, M. Sasase, M. Hara, H. Hosono, Direct activation of cobalt catalyst by 12CaO center dot $7Al_2O_3$ electride for ammonia synthesis, ACS Catal. 9 (2019) 1670–1679.
[48] D. Wrana, K. Cieslik, W. Belza, C. Rodenbucher, K. Szot, F. Krok, Kelvin probe force microscopy work function characterization of transition metal oxide crystals under ongoing reduction and oxidation, Beilstein J. Nanotechnol. 10 (2019) 1596–1607.
[49] Y.X. Yang, J. Zhou, M. Nakayama, L.Z. Nie, P. Liu, M.G. White, Surface dipoles and electron transfer at the metal oxide-metal interface: a 2PPE study of size-selected metal oxide clusters supported on Cu(111), J. Phys. Chem. C 118 (2014) 13697–13706.